Rock Mechanics and Rock Engineering (2019) 52:133–147
https://doi.org/10.1007/s00603-018-1587-x

ORIGINAL PAPER

Numerical Modelling of Water Flow Through Granular Material for Isolated and Simultaneous Extractions in Block Caving

Katherine Sánchez[1,2] · Sergio Palma[1,3,4] · Raúl L. Castro[1,2]

Received: 23 January 2018 / Accepted: 29 August 2018 / Published online: 4 September 2018

Abstract

In this work, we numerically solve the Brinkman–Darcy equation coupled to the granular kinematic model using the finite elements method in 2D, to describe the entry of water into draw points in Block Caving mining. We perform a total of 990 numerical simulations incorporating the relative change of local rock density ($\Delta\rho/\rho_p$), particle size (D_p), extraction area (S) and the separation between draw points (L). We propose two mathematical models using scale arguments for estimating the velocity of the water in the draw point as a function of two and three dimensionless numbers (for isolated and simultaneous extractions, respectively). The relative error in the estimation of the results using the mathematical model for the set of numerical experiments ranges from 0.83 to 6.09%, where the greatest deviations correspond to $D_p = 6$ mm. The proposed models allow estimating the water velocity at the draw point, which in turn helps to predict the time and place where there is a greater probability of a mud rush occurrence. The results can be applied in the design and optimisation of extraction sequences when the water present in the subsoil of a mine is a relevant factor to consider.

Keywords Block caving · Mud rush · Porous medium · Brinkman–Darcy equation · Granular materials · Kinematic model

Abbreviations

$\vec{u}$	Velocity field of the fluid (m/s)
K	Hydraulic conductivity, (m^2)
∇	Gradient of the hydraulic head (m^{-1})
ϕ	Porosity of the medium
ρ	Fluid density (kg/m^3)
k	Intrinsic permeability of the medium, (m/s)
μ	Dynamic fluid viscosity (Pa s)
g	Gravitational constant (m/s^2)
D_p	Size grain (m)
Re	Reynolds number
υ	Kinematic viscosity (m^2/s)
τ	Stress tensor (MPa)
∇P	Gradient of the fluid pressure (MPa/m)
u_{xp}	Horizontal velocity of particles (m/s)
u_{yp}	Vertical velocity of particles (m/s)
C	Constant along streamlines
π	Pi number
e	Euler's number
ρ_p	Density of the medium (particles) inside the IMZ (kg/m^3)
$\Delta\rho$	Local density change introduced by the rock motion (kg/m^3)
ρ_0	Initial density or outside of the IMZ (kg/m^3)
Q	Extraction rate (e.g. in 2D m^2/day or in 3D m^3/day)
H_{IEZ}	Height of the isolated extraction zone (m)
W_{IEZ}	Width of the isolated extraction zone (m)
$\overrightarrow{v_F}$	Velocity of the dilation front (m/s)
$\overrightarrow{v_p}$	Particles velocity (m/s)
$\mathrm{d}y_f$	Displacement of the dilation front velocity (m)
H_{IMZ}	Height isolated movement zone (m)
W_{IMZ}	Width isolated movement zone (m)
β	Convective velocity vector (m/s)
D	Diffusion coefficient (m^2/s)
F	Arbitrary source term
c_{art}	Artificial diffusion coefficient
δ_{id}	Tuning parameter of the artificial diffusion
h	Mesh element size (m)

✉ Sergio Palma
sergio.palma.m@gmail.com

[1] Advanced Mining Technology Center, University of Chile, Santiago, Chile

[2] Block Caving Laboratory, Department of Mining Engineering, University of Chile, Santiago, Chile

[3] School of Civil Engineering, The University of Queensland, Brisbane, Australia

[4] Aix-Marseille Université, CNRS, IUSTI, Marseille, France

1 Introduction

The depletion of high-grade ore bodies near surface is a crucial issue for mining companies in times of increasing demand for metal. The alternative considered for many surface mining operations is the transition to underground where Block, Panel, and Sublevel Caving are the main large-scale mining methods utilised for deep and low-grades massive deposits. The latter methods increase the number of operational risks, such as rock explosions, air blasts and mud rush. A mud rush is the sudden and violent entry of a wet muck flow (mixture of water and fine-grained material) into underground mining operations (Butcher et al. 2000). Caving operations are inherently susceptible to mud rush, because of their potential to accumulate surface and underground water, generation of fine-grained material (by a secondary comminution process), and the overall productive activities that provide perturbation and a download point (Jakubec et al. 2012). These events are uncommon but involve a significant adverse economic impact and loss of human lives, e.g. in England, Scotland, and the United States until 1995 on average 31 deceased persons were reported, and until 1975 a maximum of 375 fatalities in the Chasnala coal mine in Jharia, India (Vutukuri and Singh 1995). In the specific case of Diablo Regimiento and Reserva Norte divisions of Codelco (Chilean Copper Company), a total loss of about 48.95 Mt was reported until November 2013 (Navia 2014; Lara 2014).

Currently, one of the proposed control measures to prevent mud rush is the criticality matrix, which is used to decrease the extracted volume in the different zones affected by mud. Accordingly, the safety factor to extract mineralised material is calculated from results of the slump test using the Abraham cone (Vallejos et al. 2017). On the other hand, Garcés et al. (2016) proposed a probabilistic approach to deal with this problem, in which a logistic binary regression uses historical reports of mud rush to establish a multivariate predictive model considering two entry mechanisms: vertical and lateral. Unfortunately, this method can only be applied in mining operations where mud rush has already occurred, while in other areas with potential risk the magnitude or timing of such events cannot be determined.

In the last two decades, research regarding water-mud flow problems has focused on establishing the fundamentals of mud rush, failure mechanisms and mitigation operational practices (Call and Nicholas 1998; Butcher et al. 2000, 2005; Samosir et al. 2008; Wicaksono et al. 2012; Widijanto et al. 2012; Holder et al. 2013; Jakubec et al. 2012; Lara 2014; Navia 2014; Valencia et al. 2014; Hekmat et al. 2016; Castro et al. 2017; Vallejos et al. 2017). Despite this constraint, questions about the dynamic behaviour of groundwater flow in these events, how the triggering mechanism act (dynamic or static), and the predictability of occurrence of mud rush events remains unresolved.

The water is the mud transport mechanism (Butcher et al. 2005), but one can hardly obtain a measurement of velocity, viscosity and pore pressure of the groundwater flow both in cave mining operations or in physical models, and also the nonlinearities of the governing equations (Nguyen 1995) lead to an unpredictable behaviour of mud rush events. Another complexity concerns the differential porosity developed by the gravity-driven granular flow (Castro et al. 2007; Hancock et al. 2012) in response to decompaction and dilatation effects during the extraction of the granular material in underground Block, Panel, and Sublevel Caving exploitation methods.

In this paper, we present a deterministic approach in which we model the behaviour of underground water coupled to the evolution of the caving, integrating equations of groundwater flow (Brinkman equation) and granular medium (modified-kinematic model), to simulate the movement of water through the muckpile or column of broken material inside the caved zone, and to estimate the inflow velocity at the draw point. For the discretisation of the equations that control the transport of water in a porous medium, the Finite Element Method (FEM) is adopted in this study because it has a mathematical formulation especially for non-linear partial differential equations and it is more accurate than Finite Volume Methods (FVM) and Finite Difference Methods (FDM). The model presented here represents a simplification of the physics of the problem since we do not consider the anisotropy of the medium, fractures network, and the dynamic of aquifers. However, we attempt to obtain a mathematical model to help us to address two main questions:

1. Which factors control the water flow and what are their relative influences?
2. What is the predicted flow velocity of water at the draw point (extraction point built below the ore for recovering it after it is caved)?

In the following sections, we first describe the equations, which control the phenomenon and then the numerical methodology. Finally, we present the results of the numerical experiments and the mathematical model obtained.

2 Governing Equations

2.1 Fluid Dynamics

A porous medium consists of a solid matrix with interconnected voids (pores), which allows the flow of one or more

fluids through the material. The movement of water through a porous medium can be modelled in the fundamental microscale by Stokes' equation, and in a macroscopic level by Darcy's law (Durlofsky and Brady 1987). Since a macroscopic approach is the most feasible way to model transport, in 1856, Darcy experimentally measured the resistance to the flow caused by the porous zone. That is, $\vec{u} = -K\nabla h$ where the velocity field of the fluid is $\vec{u}$, ∇h corresponds to the gradient of the hydraulic head and K to the hydraulic conductivity, a property of the geological setting. For a laminar flow in porous medium, Darcy's law yields a good approximation for the momentum equation (Bear 1988; Ghidaoui and Kolyshkin 1999).

The continuity equation for an incompressible fluid written in vector notation is described as

$$\frac{\partial(\phi\rho)}{\partial t} + \nabla \cdot \left(\rho\vec{u}\right) = 0. \tag{1}$$

The hydraulic conductivity, defined as the measure of the ease of a porous medium to transmit water, is a function of the lithology, texture and granulometry of the medium (Tuller and Or 2002; Fitts 2012). The hydraulic conductivity has a strong dependence on the degree of water saturation, and according to Kasenow (2002), is expressed mathematically as follows: $K = k\mu/\rho g$, where μ is the dynamic fluid viscosity (Pa s), ρ is the fluid density and g corresponds to the gravitational constant. The specific permeability or intrinsic permeability of the medium (k) represents the ability of a fragmented material to allow a fluid to pass through it (Dullien 1992), and depends on the physical properties of the porous medium, as well as on the geometry. It is independent of the nature of the fluid (Nield and Bejan 2006) and can be expressed as, $k = \alpha\phi D_p^2$, where α is a dimensionless constant related to the configuration of the medium, ϕ the porosity of the medium and D_p the size grain (Vuković and Soro 1992).

According to experimental results, Darcy's law is valid when the Reynolds number (Re) ranges between 1 and 10 (Todd 1980; Bear and Bachmat 1990; Arora 2009; Bear and Cheng 2010; Alabi 2011), which for a porous medium is defined as (Van Golf-Racht 1982),

$$\mathrm{Re} = \frac{5 \times 10^{-3}}{\phi^{5.5}} \frac{u\sqrt{K}}{v}, \tag{2}$$

where v is the kinematic viscosity. When the hydraulic conductivity K is low, the stress that undergoes the fluid is transmitted from one pore to other mainly by pressure because the solid matrix prevents direct viscous interaction of the fluid in separated pores (Faghri and Zhang 2006). The porous media is characterized by the so-called effective properties, such as the porosity, which was assumed according to data reported by Hancock et al. (2012). The growth of the caving generates the increase in the porosity, which requires accounting for the viscous transport in the momentum balance and introducing the velocity in the spatial directions as a dependent variable, so the Brinkman equation is used (Shamey and Zhao 2014). Brinkman's equation corresponds to an extension of Darcy's law, where the viscous term (μ) is added (Nield and Bejan 2006; Shi and Wang 2007). Brinkman's equation takes the following form:

$$\frac{\rho}{\phi}\left(\frac{\partial\vec{u}}{\partial t} + \left(\vec{u}\cdot\nabla\right)\frac{\vec{u}}{\phi}\right) = -\nabla P + \mu\nabla^2\vec{u} - \left(\frac{\mu}{K}\right)\vec{u} + \rho\vec{g}, \tag{3}$$

where P is the fluid pressure, as it is expressed in Durlofsky and Brady (1987).

The hydraulic conductivity is the parameter of greater significance in Eq. (3), since it controls the velocity of transport of fluids in a porous medium (Tuller and Or 2002). Brinkman's equation is a simplification of the Navier–Stokes equation, which can be applied only to a laminar flow in a porous medium (Dullien 1992) and for high porosity values (i.e. $\phi = 0.8$) (Durlofsky and Brady 1987; Faghri and Zhang 2006). The movement of material through the draw point generates a change of porosities that clearly splits of lower (final) and higher (initial) porosity zones separated by a stress arch (Castro et al. 2007). This is confirmed by the results of Hancock et al. (2012) where there are two main regions, one with relatively higher porosities in the shear band area of flow around the edges of the movement zone and another with lower porosities in the plug zone region. In the plug zone region, the porosity is low and Brinkman's equation reduces to Darcy's law (Durlofsky and Brady 1987; Shamey and Zhao 2014). Therefore, Brinkman's equation has the advantage of considering both viscous drag along the macroporous in a movement zone and Darcy effects within the porous medium itself (in situ rock). In this sense, Brinkman's equation is more applicable than Darcy's law (Shamey and Zhao 2014) and simpler compared to the Navier–Stokes equation (Shi and Wang 2007).

2.2 Granular Materials

In the block caving method, the extraction of minerals is based on the flow of rocks induced by gravity. In the mining context, the kinematics model has been used to calculate the shape of the isolated extracted zone (IEZ) and has been modified to introduce both a non-constant diffusion coefficient (Chen 1997) and a heuristic rule for dilation (Melo et al. 2009). The kinematic model describes the movement of the granular material, considering that a particle leaving the system creates a space, which is occupied by a particle from the top layer. Thus, a new space is generated, which is occupied by the top layer particle and so on (Mullins 1972). For the latter to occurs, it is assumed that the weight of the

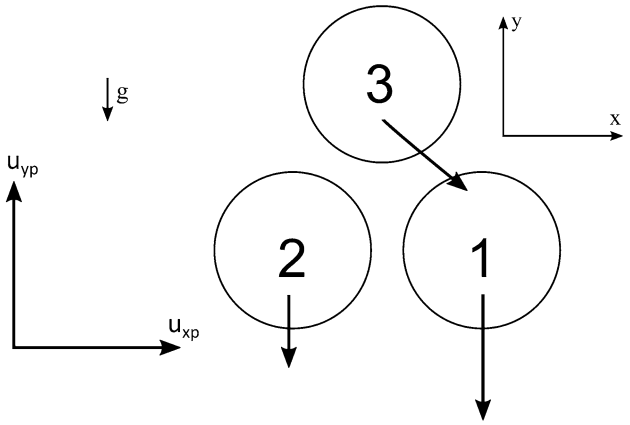

Fig. 1 The kinematics model of Nedderman and Tüzün (modified from Nedderman 2005)

particle is sufficient to cause displacement, since this does not consider stress in the system and depends exclusively on the movement and compaction of the granulated material (Nedderman and Tüzün 1979; Melo et al. 2007; Vivanco and Melo 2013). The kinematics model for predicting the velocity distribution formulated by Nedderman and Tüzün (1979), considering three particles as shown in Fig. 1, suggests that if the downward velocity of particle 1 is greater than that of particle 2, then there will be a tendency for particle 3 to move to the right, i.e. there is a relationship between the horizontal velocity u_{xp} and the gradient of the vertical velocity u_{yp}. The simplest possible relationship is given by (Nedderman and Tüzün 1979):

$$u_{xp} = -D_p \frac{\partial u_{yp}}{\partial x}, \tag{4}$$

with a diffusion coefficient proportional to the grain size D_p, and assuming a constant density throughout the system. Replacing the following equation into the stationary mass conservation equation, it can be expressed as:

$$\frac{\partial u_{xp}}{\partial x} + \frac{\partial u_{yp}}{\partial y} = 0. \tag{5}$$

For the vertical velocity, a diffusion-like equation is given as follows:

$$\frac{\partial u_{yp}}{\partial y} = D_p \frac{\partial^2 u_{yp}}{\partial x^2}. \tag{6}$$

Two elliptic-shape zones: the isolated extraction zone (IEZ) and the isolated movement zone (IMZ), are generated by extracting at a single draw point and considering the dilatation front effect (Kvapil 1965; Janelid and Kvapil 1966; Melo et al. 2009). The IEZ corresponds to the limiting surface from where all particles are extracted, while the latter refers to the surface that limits the zone where particles remain static (Fig. 2) (Kvapil 1965; Bergmark 1975; Rustan 2000; Kuchta 2002; Castro et al. 2007). To determine the exact shape of the IEZ, it is necessary to start with the kinematic model for the simplest configuration. In two dimensions, considering an infinitely narrow opening where a particle located in (x, y) moves towards the point of extraction, the solution of the diffusion-type equation is:

$$u_{xp} = \frac{\mathrm{d}x}{\mathrm{d}t} = \frac{-Q}{\sqrt{4\pi D_p y}} \exp\left(-\frac{x^2}{4D_p y}\right)\frac{x}{2y}, \tag{7}$$

$$u_{yp} = \frac{\mathrm{d}y}{\mathrm{d}t} = \frac{-Q}{\sqrt{4\pi D_p y}} \exp\left(-\frac{x^2}{4D_p y}\right), \tag{8}$$

where Q is the section of extracted granular material per unit of time. In two dimensions, S corresponds to the flow rate or extraction area (S) per unit of time. The detailed solution of this differential equation can be reviewed in Nedderman (2005). Thus, Eqs. (7) and (8) allow us to follow all particle trajectories as a function of the position.

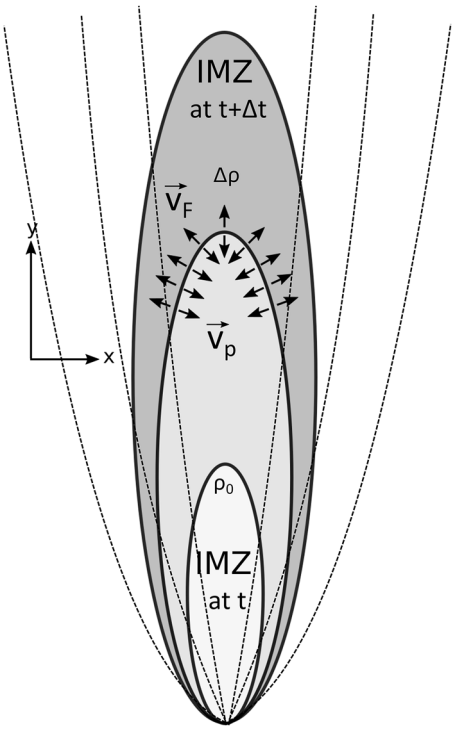

Fig. 2 Schematic model of the IEZ showing the dilatation front moving upward and the movement of particles downward once they have been reached by the IEZ [modified from Vivanco et al. (2011)]. v_p velocity of particles, v_F velocity of the dilatation front, ρ_p density inside of the IMZ, ρ_0 density outside of the IMZ, and $\Delta\rho$ local density change introduced by the rock motion

The equation for streamlines for the rock flow is given by $dx/dy = x/2y$, and its solution is $y = cx^2$, where c is a constant along a given streamline. Integrating one of the above Eqs. (7) or (8) in time and using the above streamline solution, it is possible to calculate the IEZ for a given time t, at the extraction area S. According to Melo et al. (2007, 2009), the maximum height and the maximum width of the IEZ are given by:

$$H_{\mathrm{IEZ}} = \left[\frac{3S}{4\sqrt{\pi D_p}}\right]^{2/3}, \tag{9}$$

$$W_{\mathrm{IEZ}} = 2\left(\frac{6D_p}{e}\right)\left[\frac{3S}{4\sqrt{\pi D_p}}\right]^{1/3}, \tag{10}$$

where e is the Euler's number.

This kinematics model to predict the width and height of the IEZ is in accordance with the experimental observations, but when these models are applied to the description of the IMZ, they give poor results (Melo et al. 2008, 2009), because the dilation strongly influences the size of the IMZ. This is due to the fact that granular material is in a loose packing state and when the particles start to flow as it is extracted from the opening generates local volume changes, which are not included in the original formulation of the kinematics model (Vivanco and Melo 2013). However, the IMZ is very sensitive to local packing changes because this zone defines the limit where the rocks remain static. This change depends on the sliding capacity of the rocks, which is strongly dependent on the available empty space (Melo et al. 2009). In the previous case, it is found that the original formulation of the kinematic model is not appropriate in describing the velocity distribution of particles so that a dilation front propagating upwards from the draw point was introduced. This finding has been confirmed by experimental results (Caram and Hong 1991; Samadani et al. 1999) showing that streamlines are correctly predicted by the kinematics model in a loose packing regime.

In a convergent hopper where the flow is radial, the velocity profile is described by the plasticity model (Nedderman 2005). The plasticity model can be applied to the description of the IMZ when the dilatancy effects are included and the velocity distribution is determined by the initially static stress distribution (Melo et al. 2009). The geometry of both IEZ and IMZ, in the case of radial flow described by the plasticity model, is independent of the granulate size. For greater heights, the flow cannot be considered as radial, explaining the deviation observed in the experimental curves obtained by Castro et al. (2007). This feature can be taken into account by introducing an upward propagating dilation front (Melo et al. 2008, 2009; Vivanco et al. 2011; Vivanco and Melo 2013). This dilation front is referred to a moving surface that propagates the increase in local volume caused by the packing decrease or loosening (Vivanco and Melo 2013). It is identified with the boundary of the IMZ (Castro et al. 2007; Trueman et al. 2008). Assuming a steady state flow, the mass balance of the coordinates element (x, y) located on the dilatation front at time t, can be written as

$$-J\,dt = \Delta\rho\, dy_F, \tag{11}$$

in which $J = \rho_p v_p\,(x, y)$ is the granular flow, ρ_p is the density in the grains at the steady state, v_p is the particle velocity, $\Delta\rho = \rho_0 - \rho_p$ corresponds to the local density change relative to the initial density, ρ_0 is the density outside the IMZ and dy_F is the displacement of the dilation front during the lapse time dt, which is parallel to the rock fragment velocity (Vivanco and Melo 2013). Assuming that the initial and final densities remain constant, the expression for the velocity of the dilation front can be written as

$$\frac{dy_F}{dt} = v_F = -\frac{\rho_p}{\Delta\rho} v_p. \tag{12}$$

According to Eq. (12), the dilation front moves upward faster than the rock fragments move downward. This expression represents the velocity of the dilation front in terms of the particle velocity without reference to any particular model and can be used to find the corrected form of the IEZ (Chen 1997). Replacing Eq. (6) of the vertical velocity into Eq. (12), one obtains

$$v_F = \left(\frac{\rho_p}{\Delta\rho}\right)\left[\frac{Q}{\sqrt{4\pi D_p y}}\exp\left(-\frac{x^2}{4D_p y}\right)\right]. \tag{13}$$

Then, replacing the streamline equation $y = c\left(x - x_0\right)^2$, calculated from $dy/dx = y/x - x_0$, and integrating, one has that the equation to determine the maximum height and maximum width of the IMZ of the modified-kinematic model is given by

$$H_{\mathrm{IMZ}} = \left(\frac{\rho_p}{\Delta\rho}\right)^{2/3}\left[\frac{3S}{4\sqrt{\pi D_p}}\right]^{2/3}, \tag{14}$$

$$W_{\mathrm{IMZ}} = 2\left(\frac{\rho_p}{\Delta\rho}\right)^{1/3}\left(\frac{6D_p}{e}\right)^{1/2}\left[\frac{3S}{4\sqrt{\pi D_p}}\right]^{1/3}. \tag{15}$$

Considering the local density changes through a dilation front and adding a scale factor correcting the IMZ, such that its height is reduced to a finite size, the perturbations generated by the draw process have a finite extent, improving the predictions of both the kinematics and plasticity models (Melo et al. 2008, 2009). On the other hand, the ratio of IMZ to IEZ height is dependent only on the local density

variation (Kvapil 1965; Melo et al. 2009) and the IEZ width is dependent on the granulate size due to its the linear relationship with the coefficient of diffusion, i.e. it influences the lateral diffusion of the flow (Power 2004; Melo et al. 2009).

According to Melo et al. (2008), granular materials have no intrinsic viscosity and for the mean speed of granular flow, Bagnold's law is independent of the grain size. Additionally, Bagnold's law applies to an inertial regime with a high rate of deformation (large Bagnold numbers), contrary to what happens in a block Caving process where the gravitational flow is quasi-static. Therefore, changes in the dynamic properties of water such as viscosity or Bagnold effect were not considered in this work.

In summary, Eqs. (1) and (3) are what describe the groundwater flow and Eqs. (14) and (15) of the modified-kinematic model are the equations that define the geometry of the IMZ. These are the equations utilised in the development of the numerical modelling, as indicated below.

Table 1 Set of parameters of numerical simulations

	Value
Physical parameters	
Fluid viscosity, μ (Pa s)	0.001
Fluid density, ρ (kg/m^3)	1000
Particle diameter, D_p (mm)	[2, 4, 6]
Initial fluid velocity, v_1 (mm/s)	[20, 40, 60]
Relative local density change, $\Delta\rho/\rho_p$ (%)	[1, 3, 5]
Extraction area, S (mm^2)	[4, 37, 70, 103, 136, 168, 201, 234, 267, 300]
Numerical parameters	
Separation distance between drawpoints, L mm	[140, 100, 60, 20]
Time step, Δt (s)	0.1
Simulation time, T (s)	100

3 Numerical Methodology

To investigate how significant are the changes of the water flow as the Caving develops, we conducted a series of two-dimensional numerical simulations under different physical conditions, including changes in the porosity of the material, initial water velocity, particle diameter, distance between draw points, extraction area and considering differences between the density in situ (outside IMZ) and the fragmented material (between IEZ and IMZ), that allowed us to define the fluid velocity at the draw point. The numerical model used corresponds to a set of partial differential equations (see Sect. 2), which represent a continuum in both space and time.

Equations (1), and (3) were integrated into the computational fluid dynamics and optimisation package of Comsol Multiphysics®, where they were subsequently discretised by Galerkin's finite element method (Tabatabaian 2014). In Table 1, the parameters of the numerical simulations are indicated. Figure 3 shows a simplified 2D model of an isolated draw point and a simultaneous extraction modelled in Comsol Multiphysics®, where the water source is located at the surface and enters into the system with an initial water velocity (v_1) to reach a final velocity (v_2) at the draw point. This is directly related to the opposition of the porous medium to the flow of water.

We assume the Caving development generates a variation in permeability (Table 2) due to an increased void ratio by the dilatation of material according to the extracted area (S), which is supported by numerical models of Hancock et al. (2012). We considered no-slip and no penetration in all domain borders as boundary conditions, so that $u = 0$ at the walls of the model. To select an appropriate mesh sizes for the calculations, we conducted a set of simulations for several mesh sizes under the following physical and numerical conditions: $S = 300$ mm^2, $D_p = 4$ mm and $\boldsymbol{\Delta\rho/\rho_p} = 3\%$. As shown Fig. 4, the fluid velocity for an isolated case is a function of the number of mesh elements. The same procedure was performed to analyse the convergence of the solutions for the simultaneous case, obtaining similar results. Along this line, for the discretisation of the differential equations, we chose a trade-off between the convergence and computational times with 39.938 and 68.857 free triangular elements corresponding to the isolated and simultaneous case, respectively.

The equation system was integrated from 0 to 100 s, with a time step of 0.1 s, since the transitory effect is very fast. Because Eq. (3) is a nonlinear convection–diffusion, a small amount of artificial diffusion is added (stabilisation) to obtain a more robust and faster computational performance. Comsol Multiphysics® uses three types of methods for numerical stabilisation of the general convection–diffusion transport equation for an unknown solution u, $\frac{\partial u}{\mathrm{d}t} + \beta \cdot \nabla u = \nabla \cdot (D\nabla u) + F$, (1) isotropic diffusion, (2) diffusion of streamlines and (3) crosswind diffusion. In the latter expression, the parameters β and D refer to the convective velocity term and the diffusion coefficient, respectively, while F represents an arbitrary source term (Tabatabaian 2014). It has been mathematically proven that numerical instabilities occur when the Peclet number exceeds 1. The simplest approach is to define an artificial diffusion coefficient, $c_{\mathrm{art}} = \delta_{\mathrm{id}} h|\beta|$, where h is the mesh element size, which plays an important role. Here, δ_{id} is a tuning parameter by which the amount of artificial diffusion can be adjusted. Thus, the equation is solved as $\frac{\partial u}{dt} + \beta \cdot \nabla u = \nabla \cdot \left(\left(D + c_{\mathrm{art}}\right)\nabla u\right) + F$.

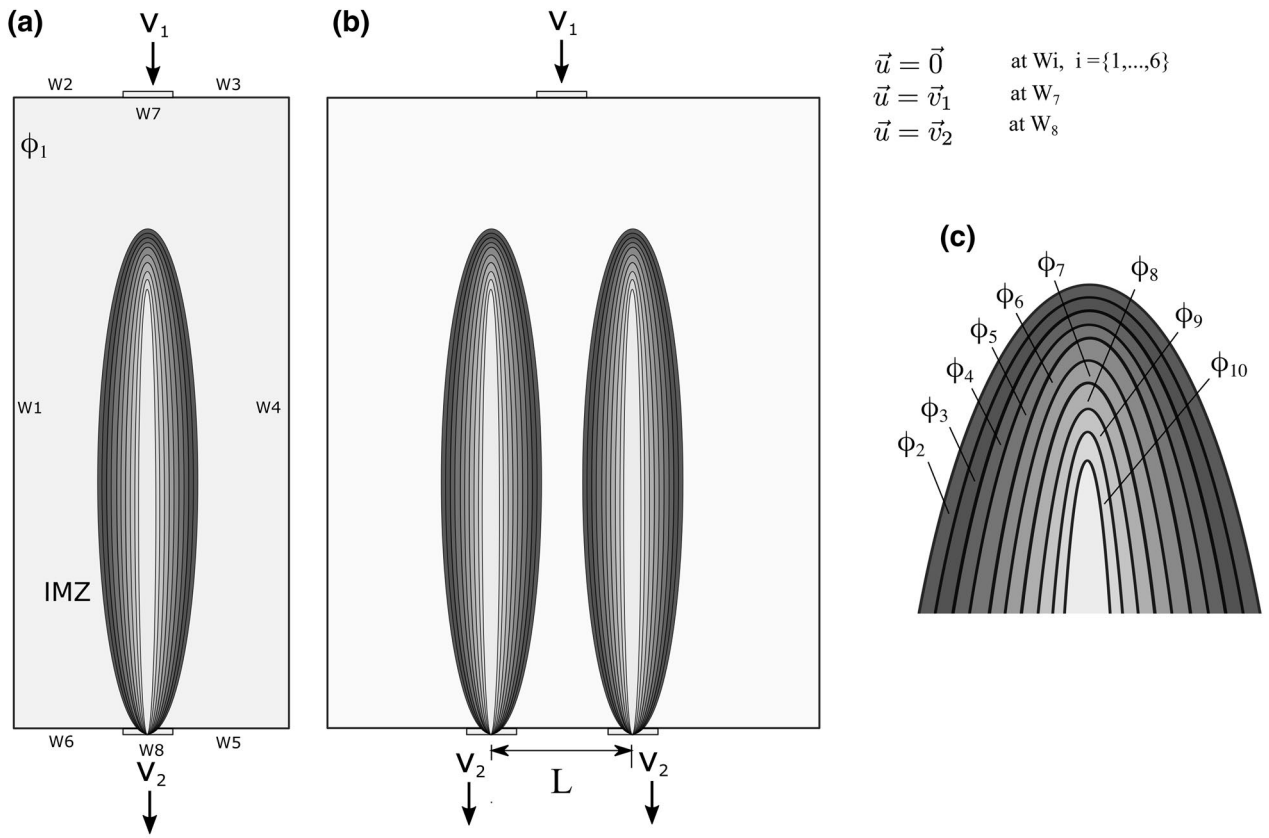

Fig. 3 Schematic conceptual model. **a** Isolated extraction. **b** Simultaneous extraction. **c** Detail of the IMZ used in the numerical simulations. The porosity of the concentric ellipses in the IMZ is represented by ϕ_j with $j \in \{1, \ldots, 10\}$. v_1 initial water velocity, v_2 final velocity, L separation distance between draw points

Table 2 Set of porosities of the ellipses

	$\phi 1$	$\phi 2$	$\phi 3$	$\phi 4$	$\phi 5$	$\phi 6$	$\phi 7$	$\phi 8$	$\phi 9$	$\phi 10$
ϕ	0.20	0.90	0.85	0.80	0.75	0.70	0.65	0.60	0.55	0.50

In some simulations, it was necessary to use a value of $\delta_{\text{id}} = 0.10$ for the convergence of all calculations. As solver convergence does not ensure that the model is numerically stable and appropriate, we verified that a closed water balance (i.e. that is not creating or destroying water numerically) is obtained from a set of numerical experiments. These numerical experiments considered the following physical and numerical conditions: $D_p = 2$ and 6 mm, $v_1 = 20$ and 60 mm/s, $S = 4$, 103, 201 and 300 mm^2, $L = 140$, 100, 60 and 20 mm and $\Delta\rho/\rho_p = 1\%$. The results are indicated in Fig. 5, where mass storage or balance is 0 (kg/s) over the entire simulations, for all cases analysed, suggesting that no water is created or destroyed and the model is appropriate and numerically stable. To capture the full interaction mechanisms between the water flow and Caving operation, sampling points were placed at the draw point, along the width and height of the IMZ and interaction zone of the ellipses, obtaining valuable information on the behaviour for different initial conditions. A physical validation of the result is given in the next section.

4 Results and Discussion

From the combination of each of the parameters listed in Table 1, the maximum number of simulations was obtained for the case of isolated and simultaneous extractions, with 270 and 720 possible numerical experiments, respectively. Our results suggest that the dynamic behaviour of the velocity of the water flow is intrinsically influenced by the development of Caving and the geometry of the IMZ, which control the magnitude of the velocity at the draw point, which in turn is directly influenced for the material removed. These findings were validated

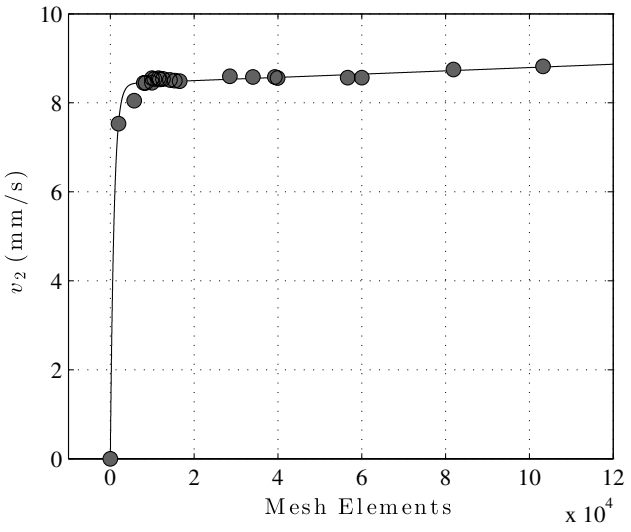

Fig. 4 Convergence of free triangular mesh. v_2 as a function of the number of mesh elements. The numerical conditions are $S = 300$ mm^2, $D_p = 4$ mm, $v_1 = 20$ mm/s and $\Delta\rho/\rho_p = 3\%$. The solid line represents the trend points for physical conditions

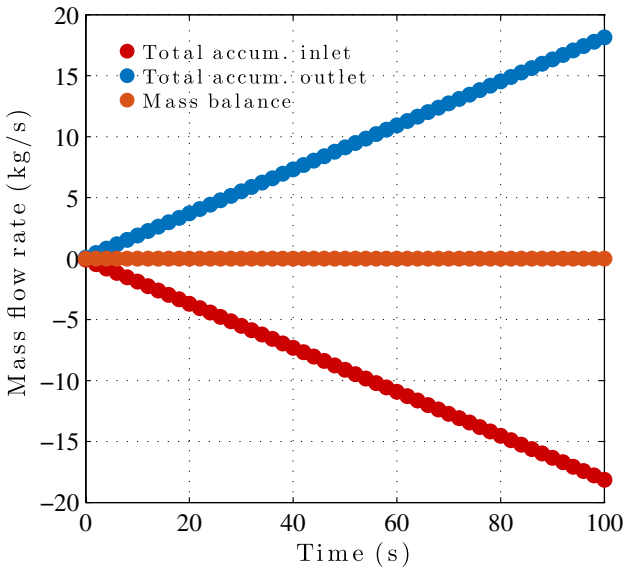

Fig. 5 Mass balance. Mass flow rate (kg/s) as a function of the simulation time. The numerical conditions are $S = 300$ mm^2, $D_p = 6$ mm, $v_1 = 60$ mm/s and $\Delta\rho/\rho_p = 1\%$. The solid line represents the mass flow rate storage of the model. (Colour figure online)

by dimensionless analysis, as the following sections will show in further detail.

4.1 Effects of the Propagation of Caving

In the case of isolated extraction with a local change in the relative density ($\Delta\rho/\rho_p$) of 1%, a granule size (D_p) of 2 mm and an initial water velocity (v_1) of 20 mm/s at a time $t = 100$ s (see Figs. 6, 9a), where t is the final time of the water flow until reaching the draw point (which must be short for an effective observation). In Fig. 9a, we observe that the decrease in the velocity field is abrupt during the transition of the first extraction period (4 mm^2) to the second (36 mm^2), decreasing at least a 55% and then a gradually decreasing (about 15% on average) in the following periods of extraction before the velocity becomes constant closer to the fourth period (103 mm^2). This is regardless of an increase in the extraction area (S) (see Figs. 6, 9a). The above velocity values were measured along the smaller diameter of the ellipse, considering that mass conservation exists.

Therefore, the results suggest that the final velocity of the water flow at the draw point (v_2) is inversely proportional to the extraction area (S), only if S is less than about half of its maximum value (300 mm^2) (Fig. 9a). In this way, the dynamic behaviour of the fluid is controlled by the surface removed in the Caving operation and the diffusion of voids, thus causing less resistance to the flow of water throughout the granular medium. The latter confirms the empirical assertion that continuous extraction drains the column of broken material at the draw point (Call and Nicholas 1998; Butcher et al. 2000; Navia 2014).

4.2 Influence of the IMZ Geometry

The geometry of the IMZ is controlled by local changes in density and the granulometry, in the case of a granular flow described by the kinematic model (Melo et al. 2009). In this way, we ran the numerical simulations considering $\Delta\rho/\rho_p = 1\%$ and D_p ranging from 2 mm to 6 mm, but with $S = 300$ mm^2 and $v_1 = 20$ mm/s as a constant for assessing the influence of the granulometry on the velocity of the water flow (see Fig. 7). In addition, we ran the numerical simulations considering $\Delta\rho/\rho_p$ to range from 1 to 5% and $D_p = 6$ mm, but with $S = 300$ mm^2 and $v_1 = 20$ mm/s as a constant, for the assessment of the influence of density changes on the velocity of the water flow (see Fig. 8).

In the first case, it is observed that increasing the size of the particle proportionally increases the width of the IMZ (see Fig. 7), and causes a reduction in water velocity at the minor axis of the IMZ. In the opposite case, a fine granulometry allows a greater transfer of the fluid because there is less resistance to the flow, and causes an increase in the expected water velocity at the draw point (v_2) by 23.31% (Fig. 9a–c). The proportionality found between the size of the particles and the width of the IMZ confirms the experimental results of Peters (1984) and Power (2004) and the conclusion of Melo et al. (2009) that the size of the material controls the lateral diffusion of gravitational flow.

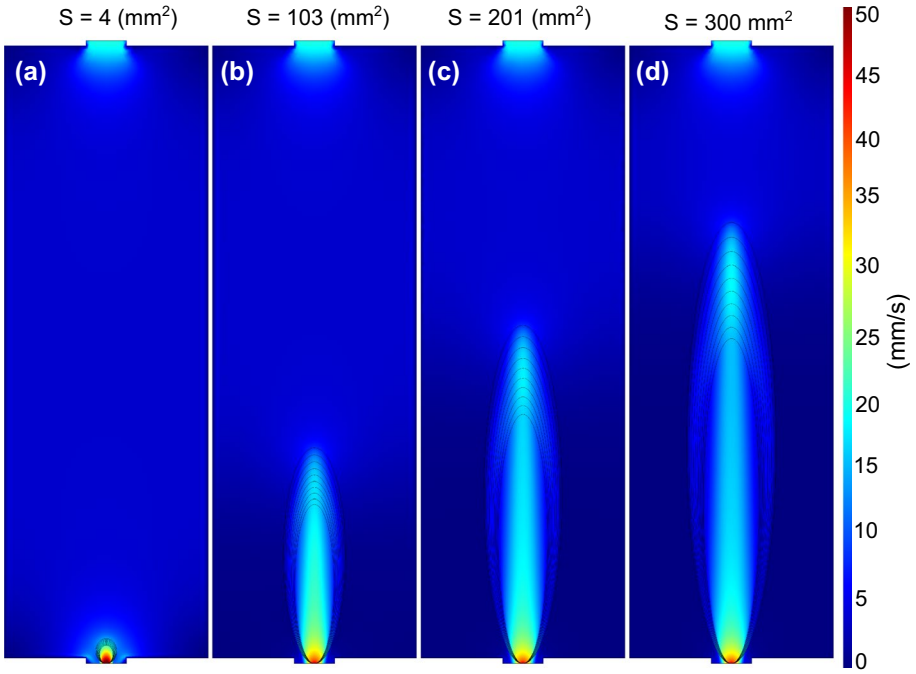

Fig. 6 Magnitude of the velocity field of an isolated draw point and evolution of the Caving for $t = 100$ s. **a** Extraction area 4 mm^2. **b** Extraction area 103 mm^2. **c** Extraction area 201 mm^2. **d** Extraction area 300 mm^2. The numerical conditions are $D_p = 2$ mm, $v_1 = 20$ mm/s, $\Delta\rho/\rho_p = 1\%$ and t is the final time of the fluid transport process. The colour bar represents the velocity of the particles. (Colour figure online)

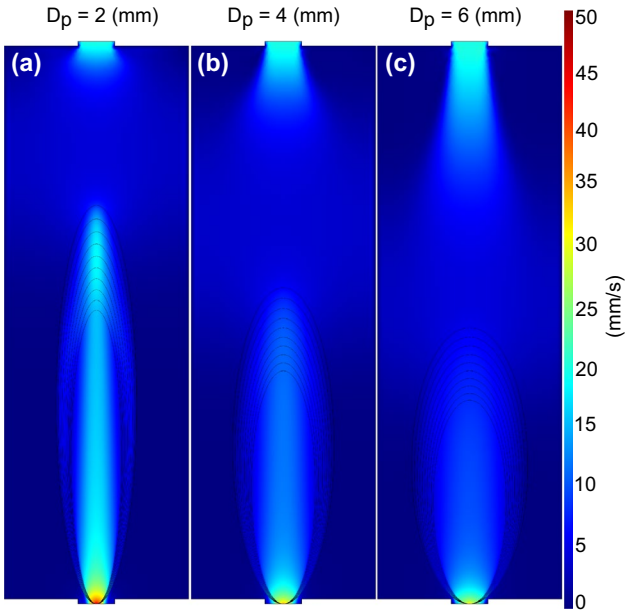

Fig. 7 Magnitude of the velocity field of an isolated draw point according to granule size for $t = 100$ s. **a** Particle size 2 mm. **b** Particle size 4 mm. **c** Particle size 6 mm. The numerical conditions are $S = 300$ mm^2, $V_1 = 20$ mm/s, $\Delta\rho/\rho_p = 1\%$ and t is the final time of the fluid transport process. The colour bar represents the velocity of the particles. (Colour figure online)

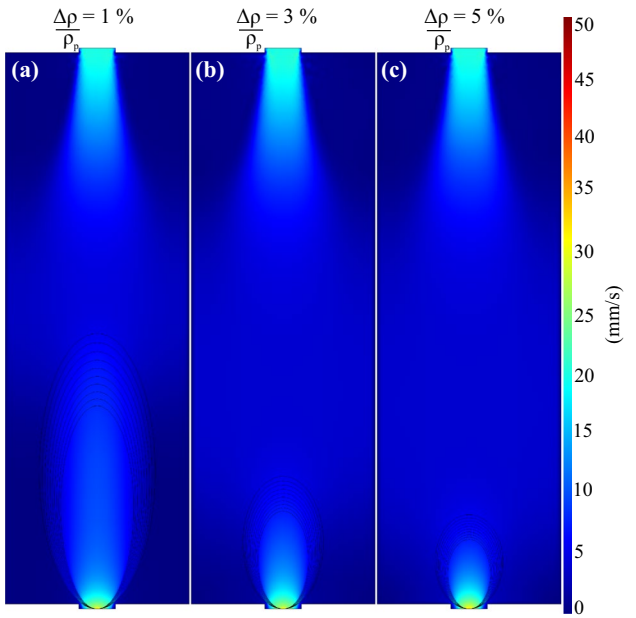

Fig. 8 Magnitude of the velocity field of an isolated draw point according to relative change of local density for, $t = 100$ s. **a** Relative change of local density 1%. **b** Relative change of local density 3%. **c** Relative change of local density 5%. The numerical conditions are $S = 300$ mm^2, $v_1 = 20$ mm/s, $D_p = 6$ mm and t is the final time of the fluid transport process. The colour bar represents the velocity of the particles. (Colour figure online)

Comparing the velocity at the draw point for different D_p and v_1 values (Fig. 9a–c), we observe that when there are larger particles, an increase of v_1 causes constant fluctuations as the extraction periods proceed and an accurate estimate of the water flow at the draw point is difficult to obtain given the erratic behaviour of the results. The fluctuations of the water flow when D_p are larger and the initial velocity (v_1) increases can be explained by the fact that flows tend to be turbulent following streamlines with abrupt changes

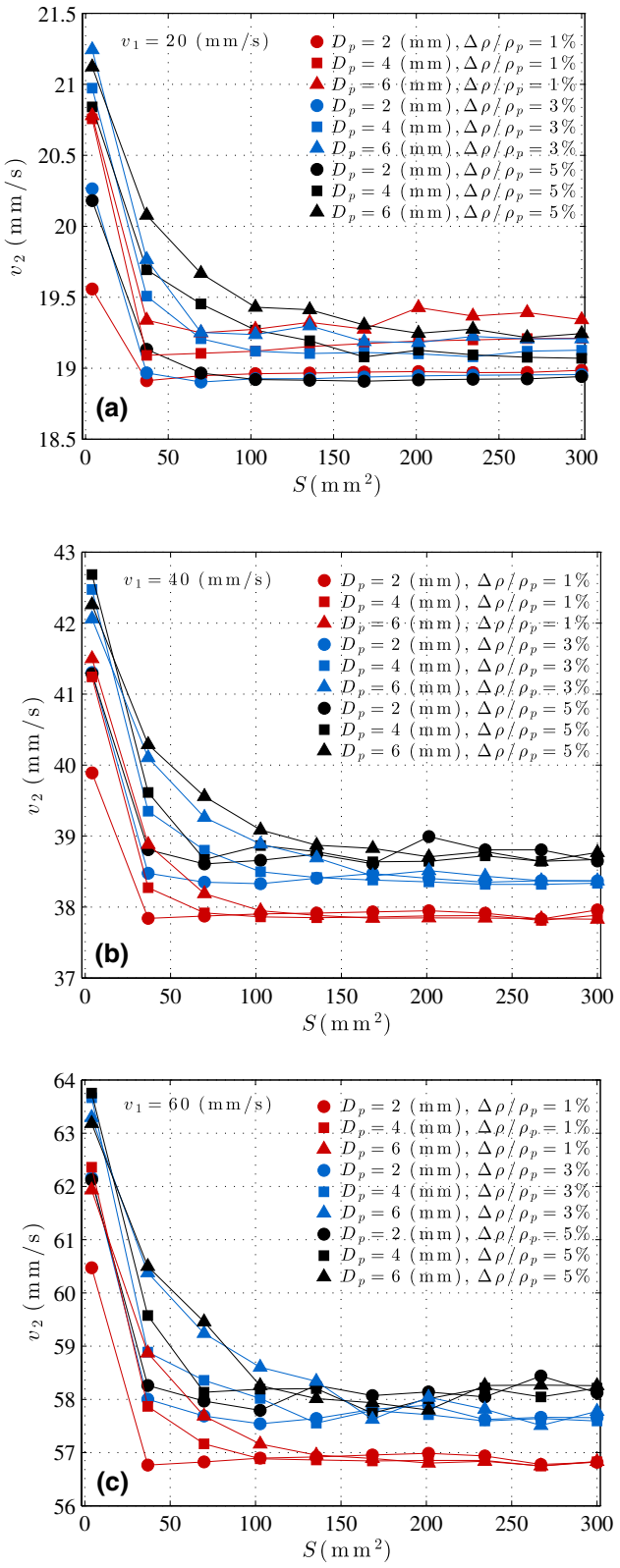

Fig. 9 Maximum magnitude of the velocity of the draw point for $\Delta\rho/\rho_p = 1\%$, $\Delta\rho/\rho_p = 3\%$ and $\Delta\rho/\rho_p = 5\%$, for $D_p = 2$ mm, $D_p = 4$ mm and $D_p = 6$ mm for $t = 100$ s as a function of extraction area, where t is the final time of the fluid transport process. The initial condition is **a** $v_1 = 20$ mm/s, **b** $v_1 = 40$ mm/s and **c** $v_1 = 60$ mm/s. The solid lines represent the numerical simulations. (Colour figure online)

of direction. The analysis also shows that for a constant S, when v_1 is low (20 mm/s), the influence of the granulometric changes on the final velocity v_2 is inhibited, such velocity being independent of the material size (see Fig. 9a). In contrast, when v_1 is high (60 mm/s) the final velocity v_2 shows well-differentiated values depending on the granulometry (See Fig. 9c).

In the second case, we observe that an increase in the relative change of the local density has a great impact on the height of the IMZ (see Fig. 8), diffusion of voids and also on the water flow at the draw point. The IMZ is smaller with an increasing difference between the density of the in situ and the fragmented material, which allows water to be transmitted easily through the latter, with little transfer to neighbouring areas due to its low permeability, increasing the fluid velocity at the minor axis IMZ up to 10.58% on average. The latter can be explained by the increasing porosity of the granular material in the IMZ that under changes of densities reduces its dimensions but also leads to increasing of the water velocity at the draw point (Castro et al. 2007).

Finally, from Fig. 9 we can observe that for $\Delta\rho/\rho_p = 3\%$ and $\Delta\rho/\rho = 5\%$, with similar S values and particularly when $v_1 = 20$ mm/s, the differences in the final velocity (v_2) are negligible. Therefore, to evaluate simultaneous extractions only the relative change of local density ($\Delta\rho/\rho_p$) between 1 and 3% is considered.

4.3 Influence of the Separation Distance Between Draw Points

Considering the numerical conditions $v_1 = 20$ mm/s, $\Delta\rho/\rho_p = 1\%$, $D_p = 4$ mm, and $S = 300$ mm^2 (as shown in Fig. 10), we can deduce that the interaction between neighbouring draw points depends on the extraction area (S) and the relative density change, but mainly on the separation distance between draw points (L). The water flow rate at the draw point increases due to the interaction between the neighbouring draw points. That is, if the draw points are located far enough apart to avoid overlapping of the IMZ's, the fluid velocity at the draw point (v_2) is close to half v_1, because they behave as two isolated draw points. If, on the other hand, they are close enough to overlap, it produces a preferential flow of water towards one of the draw points. This is because the fragmented zone favours the migration of water to the intermediate zones where there is less resistance to the flow. Subsequently, the water acquires greater velocity when approaching the draw point, where the area of influence is substantially reduced. When L decreases, we can observe a gradual decrease of the fluid velocity at the draw point with regard to the velocity at the centre of the model by 171.45% for $L = 140$ mm, 123.50% for $L = 100$ mm, 75.86% for $L = 60$ mm and 29.71% for $L = 20$ mm.

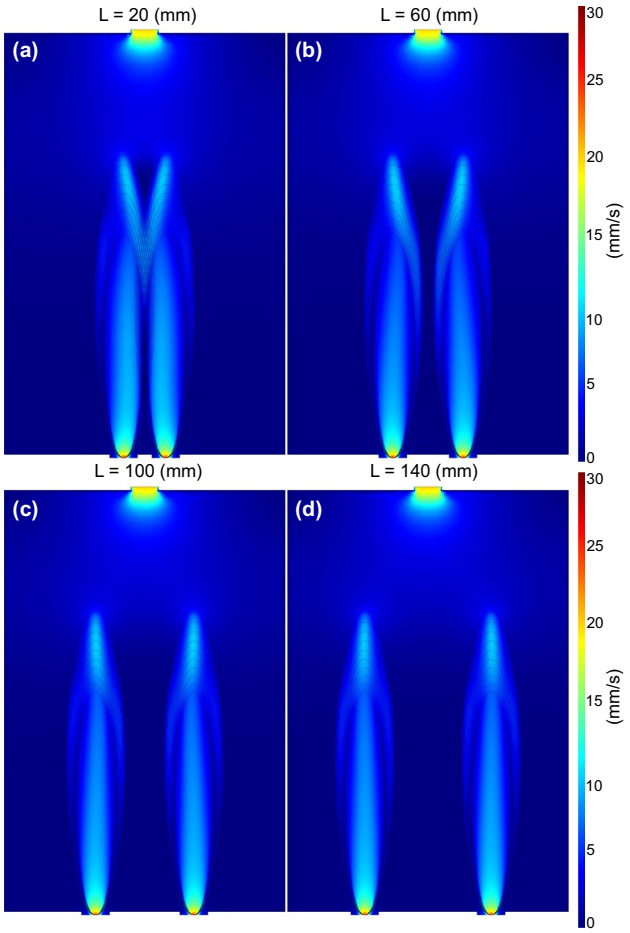

Fig. 10 Magnitude of the velocity field of the simultaneous extraction for different separation distances between draw points for $t = 100$ s. **a** Separation distance between draw point 20 mm. **b** Separation distance between draw points 60 mm. **c** Separation distance between draw point 100 mm. **d** Separation distance between draw points 140 mm. The numerical conditions are $S = 300$ mm^2, $v_1 = 20$ mm/s, $\Delta\rho/\rho_p = 1\%$, $D_p = 4$ mm and t is the final time of the fluid transport process. The colour bar represents the velocity of the particles. (Colour figure online)

4.4 Dimensional Analysis

Dimensional analysis is a method to reduce the number and complexity of variables that describe a physical phenomenon by compacting techniques, thereby making it simpler to model them (Barenblatt 1996). The application of dimensional analysis is conditional in that the physical process must satisfy the principle of dimensional homogeneity (PDH), i.e. a dimensionally correct relationship between the variables, so that the variables are independent of the system of units used (Barenblatt 1996; Szirtes 2007). Dimensional analysis is essentially a mean of utilising partial knowledge of a problem when the details are too complex and unclear to permit an exact analysis (Islam and Lye 2009). This technique has several advantages that help in the planning of experiments, provides scaling laws and savings in time and money, which can convert data from a small model to design information for a large prototype (Gibbings 2011). The method was established by Buckingham (1914), and is now called the **Π** Theorem for describing dimensionless parameters. If a physical process depends upon n dimensional variables, dimensional analysis will reduce the problem to a set of $j = n - k$ dimensionless parameters or **Π** -group, in which j scaling variables that do not form among themselves are selected, and where k is the number of physical dimensions involved. The **Π**-group will be a power product of these j variables plus one additional variable, which is assigned any convenient nonzero exponent (Buckingham 1914). Each **Π**-group thus found is independent.

Table 3 Dimensions of parameters of the numerical simulations

Variable	Dimensions
Initial water velocity (v_1) (m/s)	LT^{-1}
Final velocity (v_2) (m/s)	LT^{-1}
Particle's density (ρ_p) (kg/m^3)	ML^{-3}
Particle diameter (D_p) (m)	L
Extraction area (S) (m^2)	L^2
Distance between drawpoints (L) (m)	L

4.4.1 Isolated Extraction Case

Based on experience and on the results of the sensitivity analysis, we assumed that the water inflow rate might be described as a function of the input parameters. Each variable has an associated dimension, which can be defined as shown in Table 3.

Therefore, the formula can be written as follows, $v_2 = f(v_1, \rho_p, D_p, S, \rho_0)$. Here, $n = 6$, $k = 3$. Therefore, $j = n - k = 3$. This means there are three dimensionless numbers.

$$\Pi = \frac{v_2}{v_1}, \tag{16}$$

$$\Lambda_1 = \frac{S}{D_p^2}, \tag{17}$$

$$\Lambda_2 = \frac{\rho_0 - \rho_p}{\rho_p} = \frac{\Delta\rho}{\rho_p}. \tag{18}$$

Then, we have

$$\Pi = f(\Lambda_1, \Lambda_2). \tag{19}$$

However, if we multiply the previous dimensionless numbers, we can write another. The dimensional analysis allows us to combine dimensionless numbers. In this way, we can eliminate the previous numbers from the set of numbers and only keep the new one found.

$$\Psi = \frac{\Delta\rho}{\rho_p}\frac{S}{D_p^2}. \tag{20}$$

Finally, we get

$$\Pi = f(\Psi). \tag{21}$$

4.4.2 Simultaneous Extraction Case

This case is similar to the previous one; however, here we have the variable of separation between extraction points, $v_2 = g(v_1, \rho_p, D_p, S, \rho_0, L)$. Here, $n=7$, $k=3$. Therefore, $j=n-k=4$. This means there are four dimensionless numbers. Here, we obtain the dimensionless numbers of the previous case, Eqs. (16), (17) and (18). On the other hand, the new dimensionless can be written as,

$$\Lambda_3 = \frac{L}{D_p}. \tag{22}$$

Then, we have

$$\Pi = g(\Lambda_1, \Lambda_2, \Lambda_3). \tag{23}$$

Using the result of the previous case, we can write $\Psi_1 = \Lambda_1\Lambda_2$ and $\Psi_2 = \Lambda_3$. Finally, we get

$$\Pi = g(\Psi_1, \Psi_2). \tag{24}$$

In both cases, functions f and g must be found. To evaluate the nonlinear relationships among the variables and the groundwater flow at the draw point, we used a multidimensional Levenberg–Marquard nonlinear regression algorithm (Bard 1974). For the isolated drawpoint, the best mathematical function f that fits all the data (considering all cases under study) is given by a potential function,

$$f = \alpha_1\Psi^{\alpha_2} + \alpha_3. \tag{25}$$

Here, α_1, α_2 and α_3 are the fitting parameters. The second case is a little more complicated since the function depends on two variables and not one. The best mathematical function that fits all the data (considering all cases under study) is given by a potential function, with weak dependence on the second variable. Here, β_1, β_2, β_3 and β_4 the are fitting parameters.

$$g = \Psi_1^{[\beta_1+\beta_2\ln(\beta_3+\beta_4\Psi_2)]}. \tag{26}$$

From the data presented in Figs. 11 and 12 in the inset panel, we can infer that the dispersion of data is low and most of the data are close to the line representing the identity or perfect fit. The water velocity at the draw point that was predicted with the exponential fit, does not deviate much from the results obtained from numerical simulations, with an average relative error of 1.11% for the isolated case and 0.83% for the simultaneous case. The relative error in

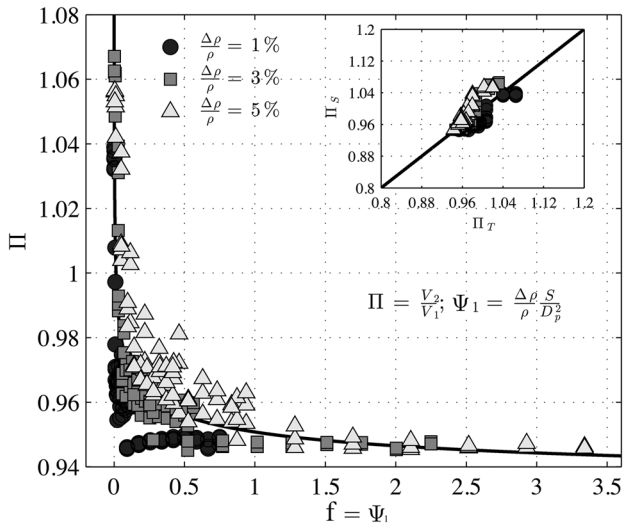

Fig. 11 Data fit for $\Pi = v_2/v_1$ as a function of the dimensionless parameter $f = \alpha_1\Psi^{\alpha_2} + \alpha_3$. Inset: data fit for v_2/v_1 simulated as a function of the theoretical v_2/v_1 proposed, Eq. (25). The solid line indicates the identity. The fitted coefficients are $\alpha_1 = 0.0281$, $\alpha_2 = -0.2389$ and $\alpha_3 = 0.9227$

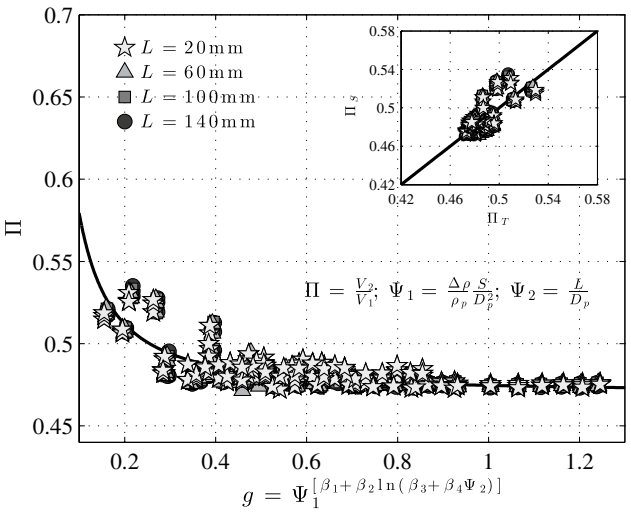

Fig. 12 Data fit for $\Pi = v_2/v_1$ as a function of the dimensionless group $g = \Psi_1^{[\beta_1+\beta_2\ln(\beta_3+\beta_4\Psi_2)]}$. Inset: data fit for v_2/v_1 simulated as a function of the theoretical v_2/v_1 proposed, Eq. (25). The solid line indicates the identity. The fitted coefficients are $\boldsymbol{\beta}_1 = 0.2867$, $\boldsymbol{\beta}_2 = -0.0034$, $\boldsymbol{\beta}_3 = -0.0006$ and $\boldsymbol{\beta}_4 = 11.5003$

the estimation of the velocity at the draw point is 56.68% for coarse-grained material (6 mm), similar to that of the isolated case (41.11%). Nevertheless, taking into account that this study represents the first numerical approximation dealing with the problem of water flow in Caving operations and considering the complexity of the hydrogeological conditions, some limitations and assumptions had to be considered to obtain the mathematical model. Therefore,

the proposed mathematical model is valid under the simplification that the medium is isotropic, homogeneous and continuous, that there is mass conservation, and laminar flow regime, which were considered to simplify the physics of the phenomenon and calculates the water flow velocity in the draw point.

5 Summary and Conclusions

The effect of ore extraction by Block, Panel and Sublevel Cave mining on groundwater flow has been evaluated through the application of Brinkman–Darcy's equation and the modified 2D kinematic model, including a front of dilatation.

From 990 numerical simulations, we determined the variables with the greatest influence on the water flow behaviour, which were dimensionally analysed by Buckingham's theorem to obtain a mathematical model that predicts groundwater flow velocity at the draw point. The proposed mathematical model presents a good fit with an average error of estimation of 0.83% and 1.11% for isolated and simultaneous extractions, respectively. The largest error in the estimation is 6.09% and corresponds to the simulations where the particle diameter is 6 mm and the relative change of local density is 3%.

The configuration developed for the numerical simulations is methodologically acceptable and the results are reliable and consistent, as they confirm the findings of Call and Nicholas (1998), Butcher et al. (2000) and Navia (2014) using constant extraction at draw points draining columns of fragmented material (muckpiles).

Our results allow us to conclude that the water flow velocity at the draw point depends on the initial water velocity, on the area of extraction (S), on the relative local density change ($\Delta\rho/\rho_p$), on the material size (D_p) and the separation distance between drawpoints (L).

An increase in S causes a sudden decrease in the final velocity of the flow (V_2), until it reaches equilibrium and acquires a constant value, approaching an exponential behaviour.

A reduction in the material size (D_p) and in the relative local density change ($\Delta\rho/\rho_p$) leads to an increase in the size of the IMZ. This in turn generates an increase in the expected water velocity at the draw point (v_2) due to the fact that the flow is dispersed more easily within the muckpile. In this regard, the existence of material of fine granulometry increases the probability of a mud rush event, since it is one of the main factors necessary for its occurrence.

The final velocity of the groundwater flow (v_2) is directly proportional to the separation distances between draw points (L). A small value of L causes a greater overlap of the IMZ, which increases the circulation paths of the water flow and dissipates its velocity. At the draw point, the final velocity will thus be considerably lower, since it loses velocity before reaching this height.

It is known that a high velocity of water flow and the existence of fine-grained material trigger mud rush events. Although our mathematical model has limitations regarding the tensional state and lateral migration of the water flow and simplifies the approach to deal with the mud rush problem, it nevertheless represents the first numerical approximation to its solution and offers an advantage in terms of productivity and accident prevention, since it allows coupling the evolution of extraction in the Caving area with estimation of the water velocity at the draw point, without the dangerous and unfavourable requirement that a mud rush event must have occurred previously.

Acknowledgements This study was financially supported by the Grant "PiensaCobre" under the auspices of the Corporación Nacional del Cobre de Chile (CODELCO) and the Centre for Mathematical Modelling (CMM) of the University of Chile. The authors are greatly grateful to the Block Caving Laboratory and Advanced Mining Technology Center (AMTC) of the University of Chile. The authors thank H. Rivera and J.P. Le Roux and Xavier Emery for providing much-appreciated comments, which helped to improve the clarity of this manuscript.

References

Alabi OO (2011) Validity of Darcy's law in laminar regime. Electron J Geotech Eng 16:27–40

Arora KR (2009) Soil mechanics and foundation engineering (geotechnical 7th engineering) edition. Standard Publishers Distributors, Delhi

Bard Y (1974) Nonlinear parameter estimation, vol 1209. Academic Press, New York

Barenblatt GI (1996) Scaling, self-similarity, and intermediate asymptotics: dimensional analysis and intermediate asymptotics, vol 14. Cambridge University Press, Cambridge

Bear J (1988) Dynamics of fluids in porous media. Dover Publications Inc, New York

Bear J, Bachmat Y (1990) Introduction to modeling phenomena of transport in porous media. Kluwer, Dordrecht

Bear J, Cheng AHD (2010) Modelling groundwater flow and contaminant transport, vol 23. Springer, Amsterdam

Bergmark JE (1975) The calculation of drift spacing and ring burden for sublevel caving. LKAB memo # RU 76-16

Brinkman HC (1947) A calculation of the viscosity and the sedimentation constant for solutions of large chain molecule staking into account the hampered flow of the solvent through these molecules. Physica 13:447–448

Buckingham E (1914) On physically similar systems: illustrations of the use of dimensional equations. Phys Rev 4:345–376

Butcher R, Joughin W, Stacey TR (2000) Methods of combating mudrushes on diamond and base metal mines. Safety in Mines Research Advisory Committee (SIMRAC), Johannesburg

Butcher R, Stacey TR, Joughin WC (2005) Mud rushes and methods of combating them. J S Afr Inst Min Metall 105:817–824

Call and Nicholas(1998) IOZ wet muck study. PT Freeport internal report **(Unpublished)**

Caram H, Hong DC (1991) Random-walk approach to granular flows. Phys Rev Lett 67:828–831
Castro R, Trueman R, Halim A (2007) A study of isolated draw zones in block caving mines by means of a large 3D physical model. Int J Rock Mech Min Sci 44:860–870
Castro R, Basaure K, Palma S, Vallejos J (2017) Geotechnical characterization of ore related to mudrushes in block caving mining. J S Afr Inst Min Metall 117:275–284
Chen G (1997) Stochastic modeling of rock fragment flow under gravity. Int J Rock Mech Min Sci 34:323–331
Dullien FA (1992) Porous media: fluid transport and pore structure, 2nd edn. Academic Press, San Diego
Durlofsky L, Brady JF (1987) Analysis of the Brinkman equation as a model for flow in porous media. Phys Fluids 30:3329–3341
Faghri A, Zhang Y (2006) Transport phenomena in multiphase systems, 1st edn. Academic Press, San Diego
Fitts CR (2012) Groundwater science, 2nd edn. Academic Press, San Diego
Garcés D, Castro R, Valencia ME, Armijo F (2016) Assessment of early mud entry risk for long term cave mining applications. 1st International Congress on Underground Mining U-Mining, Santiago, pp 428–439
Gavin H (2011) The Levenberg–Marquardt method for nonlinear least squares curve-fitting problems. Course lectures:experimental systems. Department of Civil and Environmental Engineering, Duke University, Durham. http://people.duke.edu/~hpgavin/ce281/lm.pdf Accessed 31 May 2017
Ghidaoui MS, Kolyshkin AA (1999) Some global properties of flow in a heterogeneous isotropic porous medium. Mech Res Commun 26:161–166
Gibbings JC (2011) Dimensional analysis. Springer, London
Hancock W, Weatherley D, Chitombo G (2012) Modeling the gravity flow of rock using the discrete element method. In: Proceedings of the sixth international conference and exhibition on mass mining, Canadian Institute of Mining, Metallurgy and Petroleum, 6972, Ontario
Hekmat A, Castro R, Navia I, Sánchez LK, Palma S (2016) Mud inflow risk assessment in block caving operation based on AHP comprehensive method. In: Proceedings of risk and resilience mining solution, Vancouver
Holder A, Rogers AJ, Bartlett PJ, Keyter GJ (2013) Review of mud rush mitigation on Kimberley's old scraper drift block caves. J S Afr Inst Min Metall 113:529–537
Islam MF, Lye LM (2009) Combined use of dimensional analysis and modern experimental design methodologies in hydrodynamics experiments. Ocean Eng 36:237–247
Jakubec J, Clayton R, Guest A (2012) Mud rush risk evaluation. In: Proceedings of the sixth international conference and exhibition on mass mining, Canadian Institute of Mining, Metallurgy and Petroleum, 6860, Ontario
Janelid I, Kvapil R (1966) Sublevel caving. Int J Rock Mech Min Sci Geomech Abstr 3:129–132
Kasenow M (2002) Determination of hydraulic conductivity from grain size analysis. Water Resources Publication, LLC, Denver
Kuchta ME (2002) A revised form of the Bergmark-Roos equation for describing the gravity flow of broken rock. Miner Resour Eng 11:349–360
Kvapil R (1965) Gravity flow of granular materials in hoppers and bins in mines—II. Coarse material. Int J Rock Mech Min Sci Geomech Abstr 2:277–292
Lara N (2014) Análisis histórico de las variables operacionales asociadas al ingreso de agua-barro en el sector Reserva Norte, División El Teniente, Codelco. Dissertation, Universidad de Chile
McCarthy PL, Harvey S (1998) Inrushes and subsidence, vol 3. Australasian Institute of Mining and Metallurgy, Queensland
McNearny RL, Abel JF (1993) Large-scale two-dimensional block caving model tests. Int J Rock Mech Min Sci Geomech Abstr 30:93–109
Melo F, Vivanco F, Fuentes C, Apablaza V (2007) On drawbody shapes: from Bergmark–Roos to kinematic models. Int J Rock Mech Min Sci 44:77–86
Melo F, Vivanco F, Fuentes C, Apablaza V (2008) Kinematic model for quasi-static granular displacements in block caving: dilatancy effects on drawbody shapes. Int J Rock Mech Min Sci 45:248–259
Melo F, Vivanco F, Fuentes C (2009) Calculated isolated extracted and movement zones compared to scaled models for block caving. Int J Rock Mech Min Sci 46:731–737
Mullins WW (1972) Stochastic theory of particle flow under gravity. J Appl Phys 43:665–678
Navia IM (2014) Análisis del ingreso de agua-barro al sector Diablo Regimiento, División El Teniente. Dissertation, Universidad de Chile
Nedderman RM (2005) Statics and kinematics of granular materials, 2nd edn. Cambridge University Press, Cambridge
Nedderman RM, Tüzün U (1979) A kinematic model for the flow of granular materials. Powder Tech 22:243–253
Nguyen HD (1995) Probabilistic modeling of moisture flow in layered vadose zone: applications to waste site performance assessment. Int J Eng Sci 33:1345–1355
Nield DA, Bejan A (2006) Convection in porous media, 3rd edn. Springer, New York
Palmstrom A, Stille H (2007) Ground behaviour and rock engineering tools for underground excavations. Tunn Undergr Space Tech 22:363–376
Peters DC (1984) Physical modeling of the draw behavior of broken rock in caving. Colo Sch Mines Q 79:1
Power GR (2004) Modelling granular flow in caving mines: large scale physical modelling and full scale experiments. Dissertation, The University of Queensland
Rustan A (2000) Gravity flow of broken rock: What is known and unknown. In: Proceedings of the third international conference and exhibition on mass mining, The Australasian Institute of Mining and Metallurgy, Brisbane, pp 557–568
Samadani A, Pradhan A, Kudrolli A (1999) Size segregation of granular matter in silo discharges. Phys Rev E 60:7203. https://doi.org/10.1103/PhysRevE.60.7203
Samosir E, Basuni J, Widijanto E, Syaifullah T (2008) The management of wet muck at PT Freeport Indonesia's deep ore zone mine. In: Proceedings of the fifth international conference and exhibition on mass mining, LuleåUniversity of Technology, Luleå, pp 323–332
Schlegel F (2014) Understanding stabilization methods. Comsol blog: technical content. COMSOL, Inc., Burlington. https://www.comsol.com/blogs/understanding-stabilization-methods. Accessed 14 Aug 2018
Shamey R, Zhao X (2014) Modelling, simulation and control of the dyeing process. Woodhead Publishing, New York
Shi Z, Wang X (2007) Comparison of Darcy's law. the Brinkman equation, the modified NS equation and the pure diffusion equation in PEM fuel cell modeling. In: Proceedings of the COMSOL conference 2007, Boston
Szirtes T (2007) Applied dimensional analysis and modeling, 2nd edn. Butterworth-Heinemann, Oxford
Tabatabaian M (2014) COMSOL for engineers. Mercury learning and information, Dulles
Todd DK (1980) Groundwater hydrology, 2nd edn. Wiley, New York
Trueman R, Castro R, Halim A (2008) Study of multiple draw-zone interaction in block caving mines by means of a large 3D physical model. Int J Rock Mech Min Sci 45:1044–1051
Tuller M, Or D (2002) Unsaturated hydraulic conductivity of structured porous media. Vadose Zone J 1:14–37

Valencia M, Basaure K, Castro R, Vallejo J (2014) Towards an understanding of mud rush behaviour in block-panel caving mines. 3erCongreso Internacional en Block Caving, Santiago, pp 363–371

Vallejos J, Basaure K, Palma S, Castro R (2017) Methodology for a risk evaluation of mud rushes in block caving mining. J S Afr Inst Min Metall 117:491–497

Van Golf-Racht TD (1982) Fundamentals of fractured reservoir engineering, vol 12. Elsevier, Amsterdam

Vivanco F, Melo F (2013) The effect of rock decompaction on the interaction of movement zones in underground mining. Int J Rock Mech Min Sci 60:381–388

Vivanco F, Watt T, Melo F (2011) The 3D shape of the loosening zone above multiple draw points in block caving through plasticity model with a dilation front. Int J Rock Mech Min Sci 48:406–411

Vukovic M, Soro A (1992) Determination of hydraulic conductivity of porous media from grain-size distribution. Water Resources Publications, Littleton

Vutukuri VS, Singh RN (1995) Mine inundation-case histories. Mine Water Environ 14:107–130

White FM (2008) Mecánica de fluidos, 6th edn. McGraw-Hill, New York

Wicaksono D, Silalahi K, Sryanto I, Soebari L, Ekaputra A, De Jong G (2012) Potential hazard map for the wet muck flow prevention at the deep ore zone (DOZ) block cave mine, Papua, Indonesia. In: Proceeding TPT XXI PERHAPS, pp 87–95

Widijanto E, Sunyoto WS, Wilson A, Yudanto W, Soebari L (2012) Lessons learned in wet muck management in Erstberg East Skarn system of PT Freeport Indonesia. In: Proceedings of the fifth international conference and exhibition on mass mining, Canadian Institute of Mining, Metallurgy and Petroleum, 6780, Ontario